

Analyzing Voltage Bias and Temperature Induced Aging Effects in Photonic Interconnects for Manycore Computing

Sai Vineel Reddy Chittamuru, Ishan G Thakkar, Sudeep Pasricha
Department of Electrical and Computer Engineering
Colorado State University, Fort Collins, CO, U.S.A.
{sai.chittamuru, ishan.thakkar, sudeep}@colostate.edu

ABSTRACT

Silicon photonic interconnects are being considered for integration in future networks-on-chip (NoCs) as they can enable higher bandwidth and lower latency data transfers at the speed of light. Such photonic interconnects consist of photonic waveguides with dense-wavelength-division-multiplexing (DWDM) for signal traversal and microring resonators (MRs) for signal modulation and detection. To enable MRs to modulate and detect DWDM photonic signals, carrier injection in MRs through their voltage biasing is essential. But long-term operation of MRs with constant or time-varying temperature and voltage biasing causes aging. Such voltage bias temperature induced (VBTI) aging in MRs leads to resonance wavelength drifts and Q-factor degradation, which increases signal loss and energy delay product in photonic NoCs (PNoCs) that utilize photonic interconnects. This paper explores VBTI aging in MRs and demonstrates its impacts on PNoC architectures for the first time. Our system-level experimental results on two PNoC architectures indicate that VBTI aging increases signal loss in these architectures by up to 7.6dB and increases EDP by up to 26.8% over a span of 5 years.

Categories and Subject Descriptors: [Networks] Network on chip; [Hardware] Photonic and optical interconnect; [Hardware] Process variations; [Hardware] Aging of circuits and systems; [Hardware] Emerging optical and photonic technologies

Keywords: Photonic network on chip; microring aging; thermal variations; process variations

1. INTRODUCTION

Recent advances in the integration of photonic interconnects with CMOS circuits have enabled the use of photonics for on-chip communication [1]. On-chip silicon photonic interconnects provide several prolific advantages over traditional metallic counterparts, including near light speed transfers, high bandwidth density, and low power dissipation [2]. Moreover, photonic links have several times lower data-dependent energy costs for global on-chip transfers than electrical wires, enabling the design of high-radix networks that are easier to program [3]-[4]. These advantages of photonic interconnects have catalyzed research in the area of high performance photonic NoCs (PNoCs) for manycore systems.

Permission to make digital or hard copies of all or part of this work for personal or classroom use is granted without fee provided that copies are not made or distributed for profit or commercial advantage and that copies bear this notice and the full citation on the first page. Copyrights for components of this work owned by others than ACM must be honored. Abstracting with credit is permitted. To copy otherwise, or republish, to post on servers or to redistribute to lists, requires prior specific permission and/or a fee. Request permissions from Permissions@acm.org.

SLIP '17, June 17 2017, Austin, TX, USA

© 2017 ACM. ISBN xxx-x-xxx-xxx-xx/xx...\$15.00

DOI: <http://dx.doi.org/xx.xxxx/xxxxxxx.xxxxxx>

PNoC architectures (e.g., [3]-[6]) employ multiple high-bandwidth photonic interconnects, each of which is comprised of a photonic waveguide that connects two or more nodes (e.g., cores). Typically, a large number of wavelengths are dense wavelength division multiplexed (DWDM) in a single photonic waveguide. Each wavelength corresponds to a transmission channel that is used for data transfers. Additionally, a photonic interconnect employs microring resonator (MR) modulators (that are in resonance with the utilized wavelengths) at the source node to modulate electrical signals onto photonic signals that travel through the waveguide, and MR detectors at the destination node to detect photonic signals and recover electrical signals. In general, the use of multiple wavelengths (or channels) in a photonic waveguide enables high bandwidth parallel data transfers across the waveguide.

At any point of time in a photonic waveguide, MRs can be either in-resonance or out-of-resonance with respect to the utilized DWDM wavelengths. In resonance mode, an MR couples/removes light of the resonant wavelength from the waveguide, and hence, modulates logic “0” (represented by the absence of light in the waveguide) on the resonant wavelength. In contrast, in the out-of-resonance-mode, an MR does not couple any light from the waveguide, and hence, modulates logic “1” (represented by the presence of light in the waveguide) on the resonant wavelength. Thus, a particular sequence of 1s and 0s can be modulated on a wavelength by switching the corresponding MR off and on resonance with the wavelength in the same sequence. MRs can employ either voltage biasing [7] or heating [8] to switch from resonance-mode to out-of-resonance-mode or vice versa. *However, voltage biasing is preferred over heating [8] to switch resonance-modes of MRs, as it is faster and dissipates lower power.*

To facilitate switching of resonance-modes of an MR with voltage biasing, a PN junction is created in the silicon (Si) core of the MR surrounded by silicon-di-oxide (SiO_2) cladding. A positive/negative voltage bias is applied to this PN-junction to inject/remove free carriers into/from the MR’s Si core. For high frequency operation and lower power consumption, an MR’s PN-junction is typically operated under a negative voltage bias or reverse bias [9] (otherwise known as carrier depletion mode of an MR). The application of this voltage bias generates an electric field across the MR’s Si (core) and SiO_2 (cladding) boundary. Similar to MOSFETs, this electric field generates voltage bias temperature induced (VBTI) traps at the Si- SiO_2 boundary of the MR over time (i.e., VBTI aging). Our analysis has shown that these VBTI aging induced traps alter carrier concentration in the Si core of MRs, which incur resonance wavelength drifts and increase optical scattering loss in MRs to decrease Q-factor of MRs.

In this paper, for the first time, we study the VBTI aging in MRs and its impact on PNoC architectures. At the device-level, we carefully developed analytical models for trap generation with VBTI aging in MRs. We also devise analytical models that determine variations of MR resonance wavelength shifts and Q-factor with aging-induced traps. These models are further extended

to examine the impact of different operating temperatures and bias voltages, as well as process variations. From those models, we follow a mathematical bottom-up approach to analyze the system-level impact of aging on different PNoC architectures. We present our aging analysis on well-known Corona [3] and Clos [5] PNoCs running real-world multi-threaded PARSEC [10] benchmarks.

2. RELATED WORK

Recent research on silicon photonics for manycore computing has focused on exploring a wide spectrum of network topologies and protocols to enable efficient PNoC architectures [3]-[6]. PNoCs utilize several photonic devices such as MRs as modulators and detectors, waveguides, splitters, and trans-impedance amplifiers (TIAs). The reader is directed to [11]-[13] for more discussion on these devices.

Fabrication-induced process variations (PV) impact the cross section, i.e., width and height, of photonic devices such as MRs and waveguides [14]-[15]. In MRs, PV causes resonance wavelength drifts, which can be counteracted by using device-level techniques such as voltage biasing (aka localized trimming) and heating (aka thermal tuning). On the other hand, thermal variations (TV) also alter the resonance wavelength of MRs, because of variations in refractive index of the core of MRs due to thermo-optic effects. Similar to PV, resonance wavelength drifts due to PV are compensated by voltage biasing and heating [8]. A few prior works have explored the impact of PV and TV on photonic links at the system-level [16]-[22]. In [16], a methodology to salvage network-bandwidth loss due to PV-drifts is proposed, which reorders MRs and trims them to nearby wavelengths. In [17], a thermal tuning based approach is presented that adjusts chip temperature using dynamic voltage and frequency scaling (DVFS) to compensate for chip-wide PV-induced resonance shifts in MRs. Furthermore, few PV-aware cross-layer solutions were presented in [18], [19] to mitigate crosstalk noise in PNoCs with enhancements at the device and circuit levels. In [20] a tunable laser source design is demonstrated, in which the signal power at the source is adapted to compensate for signal losses due to temperature and process variations across photonic interconnects. In addition, cross-layer solutions were presented in [21], [22] towards the design of thermally resilient PNoCs with enhancements at the circuit, architecture, and operating system (OS) levels. *All of these works ignore the harmful effects of PV and TV remedies on aging in MRs.*

Aging has become an important reliability concern for ultra-scaled semiconductor devices with significant implications for both analog and digital circuit design. The most important aging mechanisms in CMOS devices include bias temperature instability (BTI) aging and hot carrier injection (HCI) aging. BTI causes a threshold voltage increase in MOSFETs due to trap generation at the Si-SiO₂ interface [23]. Negative BTI (NBTI) is observed in pMOSFETs, and it usually dominates the positive BTI (PBTI) observed in nMOSFETs [23]. A few prior works have analyzed the impact of NBTI aging mechanisms on MOSFET devices at the device-level. Different hydrogen diffusion models are proposed in [24] to determine trap generation at the Si-SiO₂ interface of pMOSFETs. In [25] models for trap generation in the Si-SiO₂ interface of reduced cross-section MOSFETs (e.g., narrow-width planar MOSFET, triple gate MOSFET, surround-gate MOSFET) are presented. *However, none of these works considers the impact of aging on MRs and its implications on DWDM-based PNoCs.*

In view of the shortcomings of prior work, in this work we aim to analyze VBTI aging in MRs, quantify its dependence on

temperature and bias voltage, and explore its impact at the PNoC architecture level.

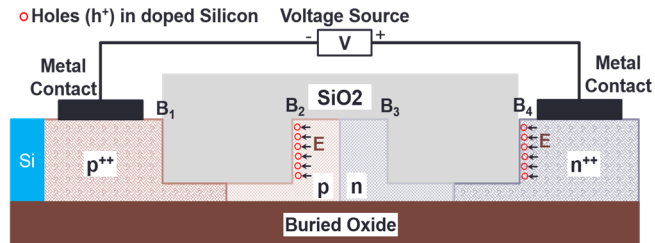


Fig. 1: Cross-section of a tunable MR with PN junction in its core to facilitate carrier injection into and removal from core with voltage biasing.

3. TRIMMING (VOLTAGE BIAS) INDUCED MR AGING

3.1 Overview of voltage bias induced trap generation in MRs

MRs, waveguides, splitters, couplers, and TIAs are basic building blocks of PNoCs [43]-[45]. MRs are essentially looped photonic waveguides with a small diameter (~a few μm), and these MRs serve as modulators to write data and detectors to read data. MRs when coupled to a waveguide in resonance-mode remove specific (resonant) wavelengths from the waveguide, whereas in the non-resonance-mode they let wavelengths simply pass through without removing them. MRs employ voltage biasing via carrier injection or removal to shift between resonance and non-resonance modes. To enable carrier injection into and removal from an MR, as shown in Fig. 1, a PN junction is created in an MR's Si core surrounded by SiO₂ cladding. To switch resonance modes at high frequency with low power dissipation using voltage biasing, an MR's PN junction needs to be reverse biased [9], which is accomplished by applying higher voltage on the n side of the PN junction (Fig. 1).

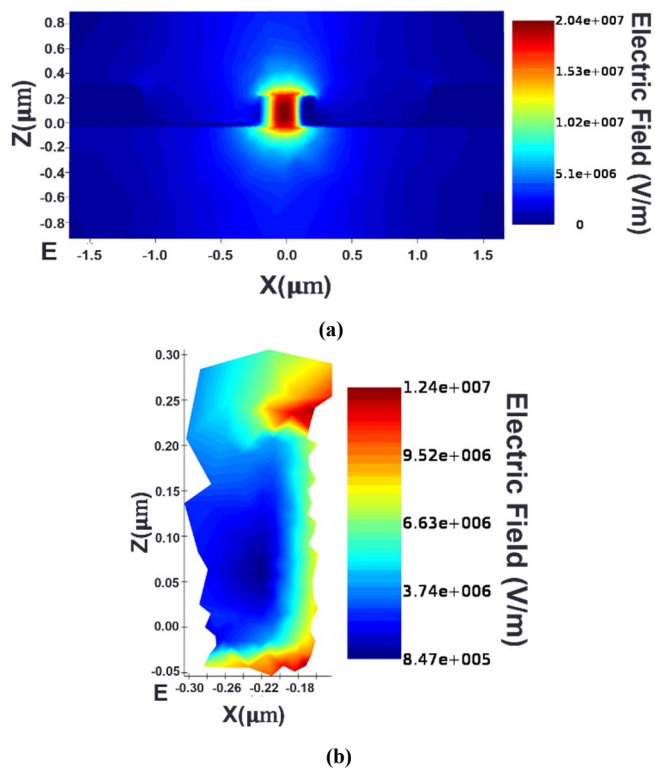


Fig. 2: Distribution of electric field (E) across (a) MR waveguide; (b) Si-SiO₂ boundary B₂ when -4V bias voltage is applied across PN junction.

When a negative voltage is applied across the PN junction of an

MR, an electric field ‘E’ is generated from right to left across the Si-SiO₂ boundaries B₁, B₂, B₃, and B₄ (Fig.1). We used the Lumerical Solutions DEVICE [26] tool to construct and model the PN junction of an MR. For our preliminary analysis, we consider an MR waveguide similar to the one reported in [27] with a radius of 2μm, fabricated using standard Si-SiO₂ material with a core cross-section of 450nm × 250nm. We then simulated the MR, using the charge transport solver in the DEVICE tool with a solver geometry of 2D y-normal, and then obtained the distribution of electric field as shown in Fig. 2 (a) across the MR waveguide with a bias voltage of -4V. The results from the DEVICE tool in Fig. 2 (a) demonstrate the presence of electric field E across all the Si-SiO₂ boundaries (i.e., B₁, B₂, B₃, and B₄). This electric field present across the Si-SiO₂ boundaries B₂ (Fig. 2(b)) and B₄ attracts holes towards them (Fig.1) and generates traps across these boundaries similar to pMOSFETs [23]. However, only the traps on the B₂ boundary change the electro-optic dynamics of the MR core as it is a boundary of the MR core. Thus in this work we focus on analyzing trap generation on the B₂ boundary.

3.2 Trap generation analytical model for MRs

The trap generation model on the B₂ boundary of an MR is based on Si-SiO₂ boundary related hydrogen dynamics [28]. The trap generation takes place at the Si-SiO₂ boundary which is a rough surface where the highly ordered Si core and the amorphous SiO₂ cladding meet. At the junction of these dissimilar materials, some of the Si atoms from the core remain dangling without satisfied chemical bonds, thus forming boundary traps. The traps generated at the Si-SiO₂ boundary of an MR are similar to the traps generated at the Si-SiO₂ boundary of a MOSFET [28]. To improve MR performance, there is a need to reduce these boundary traps. So similar to MOSFETs, MRs are annealed in ambient hydrogen during the manufacturing process. In the presence of an electric field and thermal variations across the Si-SiO₂ boundary, the Si-H bond breaks and the hydrogen gas diffuses into the MR’s SiO₂ cladding, thereby yielding passivated Si bonds (Si*) that act as traps. Furthermore, the direction of electric field (see Fig. 1) across the MR’s Si-SiO₂ boundary is similar to the direction of electric field across the MOSFET’s Si-SiO₂ boundary. Therefore, at a particular temperature both MRs and MOSFETs have a similar trap generation behavior at their respective Si-SiO₂ boundaries.

Several prior works (e.g., [23]-[25]) use reaction-diffusion (RD) models to characterize boundary trap generation at the MOSFET Si-SiO₂ boundary. As boundary traps in MR’s are similar to boundary traps in MOSFETs, we use the same RD model to model the boundary trap generation at the MR’s Si-SiO₂ boundary. This trap generation mechanism is represented as a chemical reaction in Eq. (1), where holes (h⁺) in the MR’s Si core weaken a Si-H bond and hydrogen (H) is detached [24] in the presence of electric field and thermal variations:



The generated Si dangling bond (Si*) acts as a donor-like boundary trap. The H ion released from the bond can diffuse away from the Si-SiO₂ boundary or anneal an existing trap. The boundary trap density (N_{BT}), increases with the net rate of the reaction given in Eq. (2):

$$\frac{dN_{BT}}{dt} = k_F[N_0 - N_{BT}] - k_R N_{BT} N_H \quad (2)$$

where k_F, k_R, N₀, and N_H are bond-breaking rate, bond-annealing rate, Si-H bond density available before stress, and hydrogen density at the MR’s Si-SiO₂ boundary, respectively. From Eq. (2)

it can be observed that the boundary trap generation rate increases with decrease in H ion density (N_H) at the Si-SiO₂ boundary. The diffusion of H ions away from the traps removes hydrogen from the boundary, so the boundary trap generation rate becomes limited to the diffusion rate of hydrogen. The diffusion rate of hydrogen obeys Eq. (3) [25]:

$$\frac{dN_H}{dt} = D_H \frac{d^2 N_H}{dy^2} \quad (3)$$

where D_H is the diffusion constant of hydrogen, dt is the change in time, and dy is the change in diffusion distance. During the diffusion-dominated regime, the dN_{BT}/dt term is negligible compared to the other two terms in Eq. (2) and N_{BT} is significantly smaller than N₀ [25], therefore Eq. (2) can be simplified as:

$$N_{BT} N_H = \frac{k_F N_0}{k_R} \quad (4)$$

Further, the dependence of the rate of boundary trap generation on the electric field across the boundary is included in the k_F term and the temperature dependence of trap generation is incorporated via the activation energies of k_F, k_R and D_H (see Sections 4, 5).

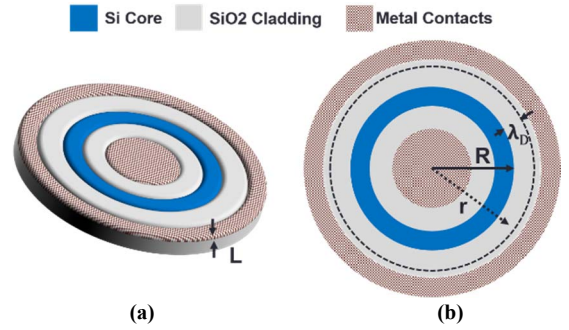


Fig. 3: (a) Microring resonator 3D-view with Si-core, SiO₂-cladding, and metal contacts for voltage biasing; (b) top view of MR which shows hydrogen diffusion length (λ_D) across its cladding.

From the RD model presented above, the number of traps generated at the Si-SiO₂ boundary is equal to the number of hydrogen ions diffused away from the boundary. But this hydrogen diffusion depends on the geometry of the boundary. The effect of the geometry of hydrogen diffusion on the trap generation rate can be analyzed with the concept of the diffusion length λ_D, which is the distance travelled by hydrogen ion into SiO₂. As outer boundary (i.e. B₂) of an MR is similar to the surround-gate cylindrical MOSFET [24], the λ_D of an MR is similar to this MOSFET. Therefore, based on estimations from prior works [24], [25] using Eq. (3) this diffusion length λ_D is estimated to be (D_H*t)^{0.5}. For the MR with outer boundary (i.e. B₂) radius R and height or thickness L depicted in Fig. 3, the hydrogen diffusion is confined within the distance R < r < R + λ_D, as shown in Fig. 3(b). To determine the total hydrogen ions available within R < r < R + λ_D, there is a need to integrate all the hydrogen ions between R and R + λ_D. Thus the hydrogen profile is expressed in cylindrical coordinates and the integral becomes:

$$N_{BT}(t) = \frac{1}{2\pi RL} \int_R^{R+\lambda_D} N_H \left(1 - \frac{r-R}{\sqrt{D_H t}}\right) 2\pi r L dr \quad (5)$$

Solving Eq. (5) and substituting N_H from Eq. (4), the interface-trap density is calculated from the geometry-dependent R–D relation as:

$$N_{BT}(t) = \sqrt{\frac{k_F N_0}{k_R}} \left(\lambda_D \left(1 + \frac{R}{\lambda_D} \right) (2R + \lambda_D) - \left(\frac{R^2 + R(R + \lambda_D) + (R + \lambda_D)^2}{3} \right)^{0.5} \right) \quad (6)$$

From the above model it is clear that trap generation on an MR's Si-SiO₂ boundary not only depends on the operational time but also on the geometry of the boundary. *These traps are the main cause of aging in MRs. In the next subsection, we analyze how such boundary trap-induced aging impacts MR optical properties.*

3.3 Aging impact on MR resonance wavelength and Q-factor

As discussed in the previous subsection, each trap generated on the core-cladding boundary of an MR consumes a hole from the P side of the MR core (Eq. (1)). Therefore, number of holes consumed in the silicon core is equal to number of boundary traps generated, which is otherwise $N_{BT} \approx -\Delta N_h$, where ΔN_h is the increase in free hole concentration and the negative sign represents decrease in free hole concentration. The removal of holes increases the refractive index of the core (n_{Si}) of a circular MR waveguide, which induces a red shift in an MR's resonance. The increase in the MR's core refractive index also increases refractive index contrast between the core and cladding ($n_{Si} - n_{SiO_2}$), which in turn increases the scattering related optical loss in the MR waveguide [30]. The increase in optical loss causes a decrease in MR Q-factor, which increases MR insertion loss. We quantify and model these phenomena in the rest of this section.

The change in hole concentration in an MR's core due to an MR aging induces refractive index change of Δn_{Si} at around 1550nm wavelength, which can be quantified as follows [29]:

$$\Delta n_{Si} = -8.8 \times 10^{-22} \Delta N_e - 8.5 \times 10^{-18} (\Delta N_h)^{0.8}, \quad (7)$$

where, ΔN_e and ΔN_h are the increase in free electron concentration and free hole concentration, respectively. Then, the increase in refractive index (positive n_{Si} as a result of aging-induced negative ΔN_h) incurs resonance wavelength red shift ($\Delta \lambda_{RWRS}$) as per the following equation [29]:

$$\Delta \lambda_{RWRS} = \frac{\Delta n_{Si} \Gamma \lambda_r}{n_g}, \quad (8)$$

where, λ_r is the initial resonance wavelength of the MR, n_g is the group refractive index (ratio of speed of light to group velocity of all wavelengths traversing the waveguide) of the MR, and Γ is the confinement factor describing the overlap of the optical mode with the MR waveguide's silicon core. The value of Γ and n_g for MR considered in our analysis are set to 0.7 and 4.2 respectively [27]. From [29], n_g accounts for refractive index dispersion and change in free carrier concentration (and hence, aging) does not significantly affect it.

An increase in the MR core's refractive index (Δn_{Si}) also increases its scattering loss coefficient. The scattering loss coefficient (that causes a fractional loss in signal amplitude) of an MR's circular waveguide is proportional to the size of the surface roughness σ , and is given by the following equation [40][41]:

$$\alpha_{scatter} = \frac{4(\cos \theta)^3 k_0^2 n_1^2 \sigma^2}{\sin \theta} \cdot \left(\frac{k_0 \sqrt{n_1^2 (\sin \theta)^2 - n_2^2}}{L k_0 \sqrt{n_1^2 (\sin \theta)^2 - n_2^2} + 2} \right) \quad (9)$$

where, k_0 is the free-space wave number at 1550nm, $n_1 = n_{Si} = 3.5$ is MR core's refractive index, $n_2 = n_{SiO_2} = 1.5$ is MR cladding's refractive index, $L = 250$ nm is the MR thickness, and $\theta = 26.51$ is the propagation angle for the fundamental mode in the MR. $\alpha_{scatter}$ corresponding to an increase in the MR core's refractive index (n_{Si}) can be evaluated from Eq. (9) by putting $n_1 = n_{Si} + \Delta n_{Si}$ in it.

The Q-factor of an MR with resonance wavelength (λ_r) depends on this scattering loss coefficient. The relation between the Q-factor and $\Delta \alpha_{scatter}$, assuming critical coupling of MRs, is given by the following equation [27], where Q_A is the loaded Q-factor of the aged MR:

$$Q_A = Q + \Delta Q = \frac{\pi n_g}{\lambda_r (\alpha + \Delta \alpha_{scatter})}, \quad (10)$$

where, ΔQ is the change in Q-factor and α is the original loss coefficient, which is the sum of three components: (i) intrinsic loss coefficient due to material loss and sidewall roughness induced scattering loss; (ii) bending loss coefficient, which is a result of the curvature in the MR; and (iii) the absorption effect factor that depends on the original free carrier concentration in the waveguide core. As explained above, aging increases the scattering loss coefficient (positive $\Delta \alpha_{scatter}$). As evident from Eq. (10), a positive value of $\Delta \alpha_{scatter}$ results in a decrease in Q-factor. This causes a broadening of the MR passband, which results in increased insertion loss.

For our VBTI aging analysis with MRs, we have considered initial original Q-factor of 9000 and loss coefficient α of 9.5cm^{-1} . As mentioned earlier, α is the sum of the scattering loss coefficient $\alpha_{scatter}$, bending loss coefficient α_b , and absorption loss coefficient α_a , the initial values of which, in this case (for $\alpha = 9.5 \text{cm}^{-1}$), are 3.5cm^{-1} , 3cm^{-1} , and 3cm^{-1} respectively. Note that $\alpha_{scatter} = 3.5 \text{cm}^{-1}$ corresponds to $\sigma = 5$ nm in Eq. (9).

4. TEMPERATURE INDUCED MR AGING

Aging in MRs is also dependent on the operating temperature (T) of the devices. As temperature alters activation energy for the Si-H bond breaking and bond annealing, it alters the bond-breaking rate (k_F) and bond-annealing rate (k_R) of the reaction shown in Eq. (1). We use the Arrhenius equation [31] to determine variation in activation energies with temperature. Eq. (11) and Eq. (12) present the temperature dependence of k_F and k_R respectively:

$$k_F = k_{F0} e^{\frac{-E_F}{K_B T}} \quad (11)$$

$$k_R = k_{R0} e^{\frac{-E_R}{K_B T}} \quad (12)$$

where, E_F and E_R are activation energies of forward dissociation and reverse annealing respectively, and K_B is the Boltzmann constant. The activation energy (E_D) of diffusion of hydrogen into the cladding of MRs also depends on temperature, which in turn alters the diffusion constant of hydrogen (D_H) as per the following equation:

$$D_H = D_0 e^{\frac{-E_D}{K_B T}} \quad (13)$$

Fig. 4 shows the variation of resonance wavelength red shift ($\Delta \lambda_{RWRS}$) and Q_A with aging in MRs at different temperatures. We analyze $\Delta \lambda_{RWRS}$ and Q_A across different operating temperatures: 300K, 350K, and 400K. From the figure it can be observed that at a particular temperature, with the increase in MR aging (i.e., increase in usage time) $\Delta \lambda_{RWRS}$ increases and Q_A decreases. With MR aging, the traps on the Si-SiO₂ boundary increase, which is evident from Eq. (6). Furthermore, change in temperature also alters k_F , k_R , and D_H as per Eq. (11), (12), and (13), respectively. These rate constants ultimately change the number of traps generated at the Si-SiO₂ boundary as per Eq. (6). An increase in number of traps incurs an increase in refractive index of an MR (see Eq. (7)), which in turn increases the MR's $\Delta \lambda_{RWRS}$ (see Eq. (8)) and scattering loss ($\alpha_{scatter}$) (see Eq. (9)). Increase in $\alpha_{scatter}$

decreases an MR's Q_A as per Eq. (10). From the figure we can also observe a higher increase in $\Delta\lambda_{RWRS}$ and higher decrease in Q_A with an increase in MR's operating temperature. As the temperature increases, the activation energy (E_D) of diffusion of hydrogen (see Eq. (13)) in the cladding of an MR decreases, which increases the diffusion rate of hydrogen and further increases trap generation at the MR core-cladding boundary. This increase in number of traps ultimately leads to higher increase in RMRS and higher decrease in Q_A .

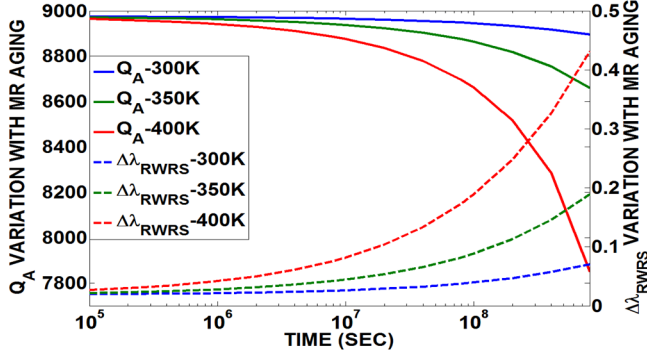


Fig. 4: Variation of resonance wavelength red shift ($\Delta\lambda_{RWRS}$) and Q_A with operation time at three operating temperatures 300K, 350K, and 400K.

5. IMPACT OF PROCESS VARIATIONS ON MR AGING

Variations in an MR's width and thickness due to process variations (PV) cause a "shift" in the resonance wavelength of the MR. As discussed earlier, voltage biasing (aka localized trimming) is essential to deal with PV-induced resonance shifts in MRs. There are other techniques such as thermal tuning that used to compensate PV-induced resonance drifts. However, thermal tuning has higher power overhead ($240 \mu\text{W}/\text{nm}$) to compensate 1nm PV-induced drift compared to localized trimming ($130 \mu\text{W}/\text{nm}$) [8]. Therefore, voltage biasing or trimming is preferred to compensate PV-induced resonance drifts over thermal tuning. Voltage biasing incurs blue shift/red shift in an MR's resonance wavelength via carrier injection/removal. To enable localized trimming in MRs to counteract PV-induced blue shifts, the negative bias voltage needs to be increased across the MR's reverse-biased PN junction. Unfortunately, this PV-induced increase in negative bias voltage results in an increase in the electric field across the MR core-cladding boundary and this electric field aggravates MR aging.

The forward dissociation constant (k_F) in Eq. (2) will depend on the electric field across core-cladding boundary (E_{OX}). Thus the equation for k_F shown in Eq. (11) is updated as per the following equation [23]:

$$k_F = B\sigma_0 E_{OX} e^{\frac{E_{OX}}{E_0}} e^{-\frac{E_F}{k_B T}} \quad (14)$$

where $\exp(E_{OX}/E_0)$ is the field dependent tunneling of holes into SiO_2 cladding, σ_0 is the capture cross-section of the Si-H bonds, and B determines field dependence of the Si-H bond dissociation.

Fig. 5 illustrates the impact of variation in bias voltage on $\Delta\lambda_{RWRS}$ and Q_A of MR with aging (i.e., usage time). We analyze negative voltage biases of 2V, 4V, 6V, and 8V, and the MR is assumed to be operated at 350K temperature. As explained Section 3.1, the charge transport solver in the DEVICE tool is used to determine electric field (E_{OX}) across the core-cladding boundary for each bias voltage across the PN junction of the MR. This tool uses MR device dimensions such as width, height and radius to determine E_{OX} at the boundary. From the figure it can be observed

that with the increase in negative bias voltage, MRs incur higher $\Delta\lambda_{RWRS}$ increase (see Eq. (8)) and higher Q_A decrease (See Eq. (9)). As the negative bias voltage across the PN junction of the MR increases, the E_{OX} across the core-cladding boundary of the MR increases. This increase in E_{OX} increases k_F as per Eq. (14), which in turn increases trap generation across the core-cladding boundary as per Eq. (6). This increase in trap generation increases $\Delta\lambda_{RWRS}$ and Q_A of an MR, as also highlighted by the Eq. (7)-(10) presented in Section 3.3.

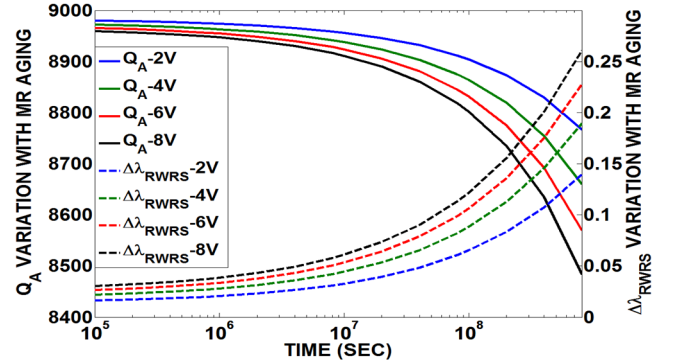


Fig. 5: Variation of Q_A and resonance wavelength red shift ($\Delta\lambda_{RWRS}$) with operation time at four bias voltages -2V, -4V, -6V, and -8V.

Table 1: Notations for photonic power loss and model parameters [12]

Notation	Parameter type	Parameter value (in dB)
L_P	Propagation loss	-0.274 per cm
L_B	Bending loss	-0.005 per 90°
L_{S12}	1X2 splitter power loss	-0.2
L_{S14}	1X4 splitter power loss	-0.2
L_{S17}	1X7 splitter power loss	-0.2
L	Photonic path length in cm	
B	Number of bends in photonic path	
λ_i	Resonance wavelength of MR	
R_{S12}	Splitting factor for 1X2 splitter	
R_{S14}	Splitting factor for 1X4 splitter	
R_{S17}	Splitting factor for 1X7 splitter	

6. IMPACT OF MR VBTI AGING ON PNOcs

6.1 MR aging analysis for Corona and Clos PNOcs

We characterize the impact of VBTI aging on two popular PNOc architectures: Corona [3] and Clos [5], both of which use DWDM-waveguides for data communication. We have considered Corona PNOc with token-slot arbitration [3] and an 8-ary 3-stage Clos PNOc [5] for our analysis. In DWDM-based waveguides, data transmission requires modulating light using a group of MR modulators equal to the number of wavelengths supported by DWDM. Similarly, data detection at the receiver requires a group of detector MRs equal to the number of DWDM wavelengths. We present analytical equations to model the impact of aging on maximum signal power loss in each architecture. Before presenting relevant equations, we provide notations for the parameters used in the equations, in Table 1.

We first model the MR transmission spectrum at a device-level and then extend these models to the system-level to determine the impact of aging on signal losses for PNOc architectures. We model the MR transmission spectrum using a Lorentzian function [32]. In Eq. (15), this function is used to represent coupling factor Φ between wavelength λ_i and an MR with resonance wavelength λ_j . Further, using the same function, we determined loss factor γ in Eq. (16), which is the factor by which signal power of a wavelength λ_i is reduced when it passes through an MR whose resonance

wavelength is λ_j . Through loss of a wavelength in a waveguide, when it passes through an MR, is defined as γ times the signal power of the wavelength before it passes through the MR. From Eq. (9) and (10), it can be inferred that an MR's loaded Q-factor (Q_A) decreases with aging in MRs. This in turn decreases Φ and increases γ as per Eq. (15) and (16), respectively. Furthermore, as per Eq. (15) and (16) increase in $\Delta\lambda_{RWRS}$ with aging (i.e., $\Delta\lambda_{RWRSi}$) further decreases Φ and increases γ , respectively.

$$\Phi(\lambda_i, \Delta\lambda_{RWRSi}, \lambda_j, Q_A) = (1 + (\frac{2Q_A(\lambda_i + \Delta\lambda_{RWRSi} - \lambda_j)}{\lambda_j})^2)^{-1}, (15)$$

$$\gamma(\lambda_i, \Delta\lambda_{RWRSi}, \lambda_j, Q_A) = (1 + (\frac{2Q_A(\lambda_i + \Delta\lambda_{RWRSi} - \lambda_j)}{\lambda_j})^{-2})^{-1}, (16)$$

Corona PNoC: This PNoC is designed for a 256 core single-chip platform, where cores are grouped into 64 clusters, with 4 cores in each cluster. A photonic crossbar topology with 64 data channels is used for communication between clusters. Each channel consists of 4 multiple-write-single-read (MWSR) waveguides with 64-wavelength DWDM in each waveguide. As modulation occurs on both positive and negative edges of the clock in Corona, 512 bits (cache-line size) can be modulated and inserted on 4 MWSR waveguides in a single cycle by a sender. A data channel starts at a cluster called 'home-cluster', traverses other clusters (where modulators can modulate light and detectors can detect this light), and finally ends at the home-cluster again, at a set of detectors (optical termination). A power waveguide supplies optical power from an off-chip laser to each of the 64 data channels at its home-cluster, through a series of 1X2 splitters. In each of the 64 home-clusters, optical power is distributed among 4 MWSR waveguides equally using a 1X4 splitter with splitting factor R_{S14} . As all 1X2 splitters are present before the last (64th) channel, this channel suffers the highest signal power loss. Thus, the worst-case signal loss exists in the detector group of the 64th cluster node, and this node is defined as the worst-case power loss node (N_{WCPL}) in the Corona PNoC. For this N_{WCPL} node, signal power ($P_{\text{signal}}(\lambda_j)$) on each detector with resonance wavelength λ_j is shown in Eq. (17). $K(\lambda_i)$ in Eq. (19) represents signal power loss of λ_i before the detector group of N_{WCPL} (see Table 1 for notations of different parameters). $\psi(\lambda_i, \lambda_j)$ in Eq. (18) represents signal power loss of λ_i before the detector with resonance wavelength λ_j in the detector group of N_{WCPL} .

$$P_{\text{signal}}(\lambda_j) = K(\lambda_i)\psi(\lambda_i, \lambda_j) \Phi(\lambda_j, \Delta\lambda_{RWRSj}, \lambda_j, Q_{A(63 \times 64 + j)}) P_{\text{in}}(i), (17)$$

$$\psi(\lambda_i, \lambda_j) = \prod_{k=1}^{(k-1) < j} \gamma(\lambda_i, \Delta\lambda_{RWRSk}, \lambda_k, Q_{A(63 \times 64 + k)}), (18)$$

$$K(\lambda_i) = (R_{S14})(L_{S14})(L_P)^L(L_B)^B \prod_{n=1}^{63} \prod_{j=1}^{64} \gamma(\lambda_i, \Delta\lambda_{RWRSn}, \lambda_j, Q_{A((n-1) \times 64 + j)}) (19)$$

Clos PNoC: An 8-ary 3-stage Clos topology is considered for a 256-core system, with 8 clusters (C1-C8) and 32 cores in each cluster. Within each cluster, a group of four cores are connected to a concentrator. Thus each cluster has 8 concentrators and the concentrators are connected electrically through a router for inter-concentrator communication. The Clos PNoC uses photonic signals for inter-cluster communication. Unlike the MWSR waveguides used in the Corona crossbar, the Clos uses point-to-point photonic links for data communication. Each point-to-point photonic link uses either forward or backward propagating wavelengths depending on the physical location of the source and destination clusters. Each photonic link in the Clos PNoC use 128

DWDM, with 64 wavelengths for forward communication and the remaining 64 wavelengths for backward communication. Thus the Clos PNoC uses only 56 waveguides with 256 MRs on each waveguide. This PNoC uses 2 laser sources to enable forward and backward communication. To power the 56 waveguides, it is assumed that the PNoC employs a series of 1X2, 1X7, and 1X4 splitters. In our implementation of the Clos PNoC, the worst-case power loss occurs when C1 sends data to C8, as this involves the longest photonic path for data traversal. Thus the node C8 is the worst-case power loss node (N_{WCPL}) in the Clos PNoC. We use Eq. (17) to determine worst-case power loss in the Clos PNoC. But as the Clos network has lower number of waveguides and fewer number of MRs on each waveguide, this in turn changes the signal power losses. Thus we modify Eq.(19) for the Clos PNoC as:

$$K(\lambda_i) = (R_{S14})(L_{S14})(L_P)^L(L_B)^B \prod_{n=1}^3 \prod_{j=1}^{64} \gamma(\lambda_i, \Delta\lambda_{RWRSn}, \lambda_j, Q_{A((n-1) \times 64 + j)}) (20)$$

6.2 Modeling PV of MR Devices in Corona and Clos PNoCs

We adapt the VARIUS tool [33] to model die-to-die (D2D) as well as within-die (WID) process variations in MRs for the Corona and Clos PNoCs. VARIUS uses a normal distribution to characterize on-chip D2D and WID process variations. The key parameters are mean (μ), variance (σ^2), and density (α) of a variable that follows the normal distribution. As wavelength variations are approximately linear to dimension variations of MRs, we assume they follow the same distribution. The mean (μ) of wavelength variation of an MR is its nominal resonance wavelength. We consider a DWDM wavelength range in the C and L bands [34], with a starting wavelength of 1550nm and a channel spacing of 0.8nm. Hence, those wavelengths are the means for each MR modeled. The variance (σ^2) of wavelength variation is determined based on laboratory fabrication data [14] and our target die size. We consider a 256-core chip with die size 400 mm² at a 22nm process node. For this die size we consider a WID standard deviation (σ_{WID}) of 0.61nm [16] and D2D standard deviation (σ_{D2D}) of 1.01 nm [16]. We also consider a density (α) of 0.5 [16] for this die size. With these parameters, we use VARIUS to generate 100 PV maps, each containing over 1 million points indicating the PV-induced resonance shift of MRs. The total number of points picked from these maps equal the number of MRs in the Corona and Clos PNoCs.

7. EXPERIMENTS

7.1 Experimental Setup

We evaluate the impact of VBTI aging on PNoCs on the Corona and Clos PNoC architectures. We modeled and performed simulation based analysis of the Corona and Clos PNoCs using a cycle-accurate NoC simulator, for a 256 core single-chip architecture at 22nm. As explained in Section 6.2, we generated 100 PV maps to evaluate MR aging impact on these PNoCs for different PV profiles. We used real-world traffic from applications in the PARSEC benchmark suite [10]. GEM5 full-system simulation [35] of parallelized PARSEC applications was used to generate traces that were fed into our cycle-accurate NoC simulator. We set a "warm-up" period of 100 million instructions and then captured traces for the subsequent 1 billion instructions. We performed geometric calculations for a 20mm×20mm chip size, to determine lengths of MWSR waveguides in the Corona PNoC and photonic links in the Clos PNoC. We consider a 5 GHz clock frequency of operation for the cores. A 512-bit packet size is utilized for both Corona and Clos PNoCs.

The static and dynamic energy consumption of electrical routers

and concentrators in the Corona and Clos PNoCs is based on results from the open source DSENT tool [36]. For energy consumption of photonic devices, we adapt model parameters from recent work [37]-[38] with 0.42pJ/bit for every modulation and detection event and 0.18pJ/bit for the driver circuits of modulators and photodetectors. We used optical loss in photonic components (Table 1) to estimate the photonic laser power budget and correspondingly the electrical laser power [42].

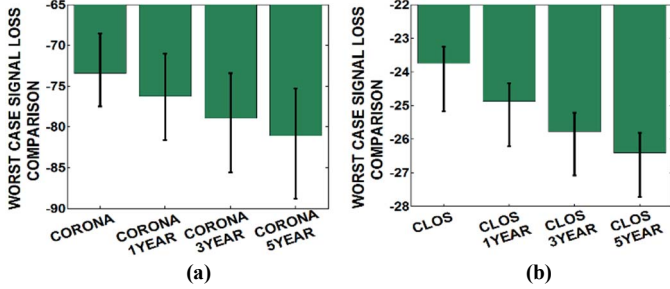


Fig. 6: Worst-case signal power loss analysis of (a) Corona PNoC and (b) Clos PNoC, with 1 Year, 3 Years, and 5 Years of aging across 100 PV maps.

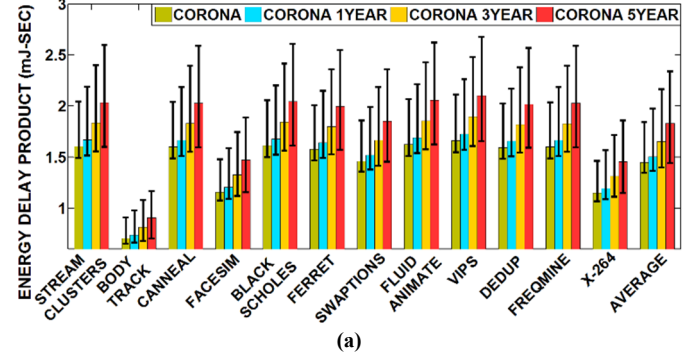
7.2 Experiment Results

Our first set of experiments compares the worst-case signal losses of the baseline Corona and Clos PNoCs with their variants with 1 Year, 3 Years, and 5 Years of VBTI aging. We have performed this aging analysis across 100 PV maps as explained in Section 6.2. The presented results are averaged across the PV maps. Furthermore, as we are determining worst-case signal loss for Corona and Clos PNoCs with VBTI aging, therefore we performed this analysis at the peak on-chip temperature, which is estimated to be 357 K [39].

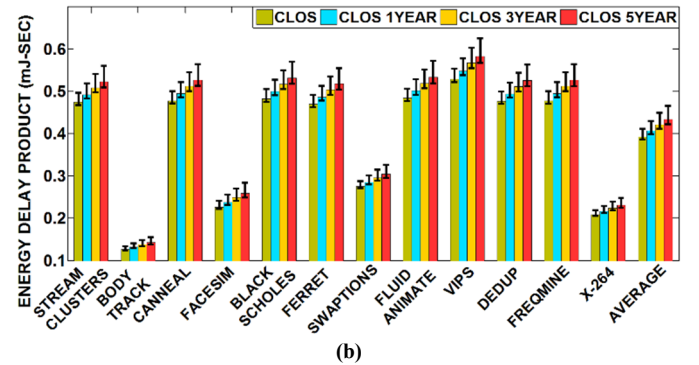
Utilizing the models presented in Section 6, we calculate the signal power loss at the last detector of the N_{WCLP} nodes of Corona and Clos PNoCs, which corresponds to the last MR detector of the cluster 64 and cluster 8 for the Corona and Clos PNoCs respectively. Fig. 6 (a) and (b) compare the worst-case signal loss of baseline Corona and Clos PNoCs with three variants of these PNoCs that undergo 1 Year, 3 Years and 5 Years of VBTI aging. The confidence intervals represent the variation in signal loss across the 100 PV maps considered. From Fig. 5(a), it can be observed that compared to their respective baselines, the Corona PNoC with 1 Year, 3 Year, and 5 years of VBTI aging has 2.8dB, 5.5dB, and 7.6dB higher signal losses, and the Clos PNoC has 1.1 dB, 2.1dB, and 2.6dB higher signal losses. The increase in resonance wavelength red shift ($\Delta\lambda_{RWRS}$) and degradation in Q-factor with VBTI aging in MRs leads to increase in MR loss factor (γ) (see Eq. (16)) and decrease in MR coupling factor (Φ) (see Eq. (15)), which ultimately increases signal losses in these PNoCs. Also, the increase in signal loss in the Corona PNoC with VBTI aging is on the higher side compared to the Clos PNoC. Corona has 16 \times higher number of MRs on its waveguides compared to the Clos PNoC, which in turn incurs higher signal losses on Corona's waveguides.

Fig. 7 (a) and (b) present detailed simulation results that quantify the energy-delay product (EDP) for the four configurations of Corona and Clos PNoCs respectively. Results are shown for twelve multi-threaded PARSEC benchmarks. From Fig. 7(a) it can be seen that on average, Corona PNoC with 1 Year, 3 Year, and 5 years of VBTI aging has 4.1%, 14.3%, and 26.8% and Clos PNoC has 3.7%, 7.5%, and 10.6% higher EDP compare to their respective baselines. Increase in worst-case signal loss with increase in VBTI

aging (see Fig. 6) contributes to an increase in the PNoCs laser power, which increases total laser energy consumption in these PNoCs. Additionally, VBTI aging in MRs has positive effects on MR trimming energy consumption, as MR aging incurs red shift in resonance wavelength which naturally reduces PV-induced blue shifts in MRs and reduces total trimming energy consumption in the PNoCs. However, these trimming energy savings are relatively on the lower side compared to the increase in laser energy consumption, which ultimately increase total energy consumption and hence the EDP.



(a)



(b)

Fig. 7: EDP comparison of (a) Corona and (b) Clos PNoCs with 1 Year, 3 Years, and 5 Years of aging considering 100 process variation maps.

From the results presented in this section, we can summarize that in Corona and Clos PNoCs, VBTI aging in MRs increases signal losses by up to 7.6dB. Despite the decrease in tuning energy consumption of the Corona and Clos PNoCs with VBTI aging, the increase in their laser energy consumption increases EDP in these architectures by up to 26.8%. The signal loss and EDP increase due to VBTI aging are much lower in architectures optimized for physical-layouts such as the Clos PNoC, than in non-optimized architectures such as Corona. PNoC architectures with more MRs per waveguide (e.g., Corona) have higher VBTI aging degradation compared to PNoC architectures with less MRs per waveguide (e.g., Clos). Thus, to reduce aging effects in a PNoC, designers should reduce the number of MRs per waveguide and increase the number of these waveguides to maintain high bandwidth.

8. CONCLUSIONS

This paper analyzed VBTI aging in MRs used in photonic interconnects, and the dependence of this aging on voltage bias and temperature. We presented an analytical model for trap generation on the MR core-cladding boundary with VBTI aging in MRs. We also consider the impact of process variations on aging. Our device-level results indicate that MR aging causes significant degradation in MR Q-factor and incurs notable resonance

wavelength red shift. We extended our MR aging analysis to the system-level for the Corona and Clos PNoCs. The system-level analysis on these PNoCs clearly shows the damaging effects of MR aging, with worst signal loss increase by up to 7.6dB and EDP increase by up to 26.8%.

9. ACKNOWLEDGMENTS

This research is supported by grants from SRC, NSF (CCF-1252500, CCF-1302693), and AFOSR (FA9550-13-1-0110).

REFERENCES

- [1] Y. A. Vlasov et al., "Silicon CMOS-integrated nanophotonics for computer and data communications beyond 100G," *IEEE Comm. Mag.*, vol. 50, no. 2, pp. 67–72, Feb. 2012.
- [2] J. D. Owens, et al., "Research challenges for on-chip interconnection networks," in *IEEE Micro*, Sep-Oct 2007.
- [3] D. Vantrease et al., "Light speed arbitration and flow control for nanophotonic interconnects," in *IEEE/ACM MICRO*, Dec. 2009.
- [4] Y. Pan, J. Kim, G. Memik, "Flexishare: Channel sharing for an energy efficient nanophotonic crossbar," in *Proc. HPCA*, 2010.
- [5] A. Joshi et al., "Silicon-photonic clos networks for global on-chip communication," in *ACM/IEEE NoCS*, May 2009, pp. 124–133.
- [6] S. V. R. Chittamuru et al., "A reconfigurable silicon-photonic network with improved channel sharing for multicore architectures," in *ACM GLSVLSI*, May 2015.
- [7] J. Ahn, et al., "Devices and architectures for photonic chip-scale integration," *Applied Physics A: MSP*, 95:989–997, June 2009.
- [8] C. Nitta, et al., "Addressing system-level trimming issues in on-chip nanophotonic networks," in *Proc. HPCA*, 2011.
- [9] P. Dong, et al., "Low Vpp, ultralow-energy, compact, high-speed silicon electro-optic modulator," in *Optics Express*, 17:22484–22490, 2009.
- [10] C. Bienia et al., "The PARSEC Benchmark Suit: Characterization and Architectural Implications," in *PACT*, Oct. 2008.
- [11] I. Thakkar, et al., "Mitigation of Homodyne Crosstalk Noise in Silicon Photonic NoC Architectures with Tunable Decoupling," in *ACM/IEEE International Conference on Hardware/Software Codesign and System Synthesis (CODES+ISSS)*, Oct. 2016.
- [12] S. V. R. Chittamuru et al., "Crosstalk Mitigation for High-Radix and Low-Diameter Photonic NoC Architectures," in *IEEE Design and Test*, 2015.
- [13] S. V. R. Chittamuru et al., "Improving Crosstalk Resilience with Wavelength Spacing in Photonic Crossbar-based Network-on-Chip Architectures," *IEEE MWSCAS*, Aug. 2015.
- [14] S. K. Selvaraja, "Wafer-Scale Fabrication Technology for Silicon Photonic Integrated Circuits," PhD thesis, Ghent University, 2011.
- [15] M. Nikdast, et al., "Modeling fabrication non-uniformity in chip-scale silicon photonic interconnects," in *DATE*, Mar. 2016.
- [16] Y. Xu et al., "Tolerating process variations in nanophotonic on-chip networks," in *Proc. ISCA*, Portland, OR, USA, 2012, pp. 142–152.
- [17] Z. Li et al., "Reliability modeling and management of nanophotonic on-chip networks," *IEEE TVLSI*, 20:98–111, 2010.
- [18] S. V. R. Chittamuru, et al., "PICO: Mitigating Heterodyne Crosstalk Due to Process Variations and Intermodulation Effects in Photonic NoCs," in *IEEE/ACM DAC*, Jun. 2016.
- [19] S. V. R. Chittamuru, et al., "Process Variation Aware Crosstalk Mitigation for DWDM based Photonic NoC Architectures," in *ISQED*, 2016.
- [20] R. Wu, et al., "Variation-Aware Adaptive Tuning for Nanophotonic Interconnects," in *Proc. of IEEE/ACM ICCAD*, 2015.
- [21] S. V. R. Chittamuru, et al., SPECTRA: A framework for thermal reliability management in silicon-photonic Networks-on-Chip, in *IEEE VLSI*, Jan 2016.
- [22] D. Dang, et al., "Islands of Heaters: A Novel Thermal Management Framework for Photonic NoCs," in *Asia and South Pacific Design Automation Conference (ASPDAC)*, 2017.
- [23] M. A. Alam, et al., "A comprehensive model for PMOS NBTI degradation," *Microelectronics Reliability*, vol. 45, 2005, pp. 71–81.
- [24] H. Kuffluoglu, "MOSFET degradation due to negative bias temperature instability (NBTI) and hot carrier injection (HCI) and its implications for reliability-aware VLSI design," PhD thesis, Purdue University, 2007.
- [25] H. Kuffluoglu, et al., "Theory of interface-trap-induced NBTI degradation for reduced cross section MOSFETs," *IEEE TED* 2006.
- [26] Lumerical Solutions Inc. – DEVICE toolkit. <https://www.lumerical.com/tcad-products/device/>
- [27] K. Preston, et al., "Performance guidelines for WDM interconnects based on silicon microring resonators", *IEEE CLEO*, 2011.
- [28] S. Ogawa et al., "Generalized diffusion-reaction model for the low-field charge build up instability at the Si-SiO2 interface," in *Phys. Review B*, vol.51, no.7, p. 4218, 1995.
- [29] R. G. Beausoleil, "Large-Scale Integrated Photonics for High-Performance Interconnects", *ACM JETC*, Vol. 7, No. 2, 2011.
- [30] M. Lipson, "Guiding, Modulating, and Emitting Light on Silicon—Challenges and Opportunities", in *JLT*, 23(12), 2005.
- [31] M. A. Alam, et al. "A comprehensive model for PMOS NBTI degradation: Recent progress," *Microelectronics Reliability*, vol. 47, 2007, pp. 853–862.
- [32] J. E. Heebner, "Nonlinear optical whispering gallery microresonators for photonics," Ph.D. dissertation, Univ. Rochester, NY, USA, 2003.
- [33] S. Sarangi et al., "Varius: A model of process variation and resulting timing errors for microarchitects," *IEEE TSM*, 21(1):3–13, 2008.
- [34] S. Xiao, et al., "Modeling and measurement of losses in silicon-on-insulator resonators and bends," in *Opt. Exp.*, 15(17),553-561, 2007.
- [35] N. Binkert et al., "The gem5 Simulator," in *CA News*, May 2011.
- [36] C. Sun, et al., "DSSENT - a tool connecting emerging photonics with electronics for opto-electronic networks-on-chip modeling," in *Proc. IEEE/ACM NOCS*, 2012.
- [37] P. Grani and S. Bartolini, "Design Options for Optical Ring Interconnect in Future Client Devices," in *ACM JETC*, May, 2014.
- [38] X. Zheng et al., "Ultra-efficient 10Gb/s hybrid integrated silicon photonic transmitter and receiver," in *Opt. Express*, Mar 2011.
- [39] M. Cho et al., "Power Multiplexing for Thermal Field Management in Many-Core Processors," in *IEEE Transactions on Components, Packaging and Manufacturing Technology*, Vol. 3, No. 1, Jan. 2013.
- [40] P. K. Tien, "Light waves in thin films and integrated optics," *Appl. Opt.*, vol. 10, no. 11, pp. 2395–2413, Nov. 1971.
- [41] *Silicon Photonics: An Introduction*. By G. T. Reed and A. P. Knights. pp. 70-75. Wiley 2004 Edition.
- [42] I. Thakkar, et al., "Run-Time Laser Power Management in Photonic NoCs with On-Chip Semiconductor Optical Amplifiers," in *IEEE/ACM International Symposium on Networks-on-Chip (NOCS)*, Aug. 2016.
- [43] S. Bahirat, S. Pasricha, "Exploring Hybrid Photonic Networks-on-Chip for Emerging Chip Multiprocessors", in *CODES+ISSS*, 2009.
- [44] S. Pasricha, S. Bahirat, "OPAL: A Multi-Layer Hybrid Photonic NoC for 3D ICs", in *ASPDAC*, 2011.
- [45] S. Bahirat, S. Pasricha, "METEOR: Hybrid photonic ring-mesh network-on-chip for multicore architectures", in *ACM Transactions on Embedded Computing Systems (TECS)*, vol. 13, no.3, March 2014.